

Crystallization Modes of Poly(3-dodecylthiophene)-based Block Copolymers Depend on Regioregularity and Morphology

Jonathan P. Coote,^{†,§} Jin-Seong Kim,^{‡,§} Byeongdu Lee,[¶] Junghun Han,[‡] Bumjoon
J. Kim,^{*,‡} and Gila E. Stein^{*,†}

[†]*Department of Chemical and Biomolecular Engineering, University of Tennessee,
Knoxville, TN 37996, USA*

[‡]*Department of Chemical and Biomolecular Engineering, Korea Advanced Institute of
Science and Technology (KAIST), Daejeon 34141, Korea*

[¶]*Advanced Photon Source, Argonne National Laboratory, Lemont, IL 60439, USA*

[§]*Equal contribution*

E-mail: bumjoonkim@kaist.ac.kr; gstein4@utk.edu

Abstract

Conjugated block copolymers (BCPs) can self-assemble into highly ordered nanostructures in a melt state. However, when cooled below the melting temperature, crystal growth can disrupt the self-assembled structure and produce a poorly-ordered fibrillar texture. We demonstrate that crystallization modes of conjugated BCPs based on poly(3-dodecylthiophene) (P3DDT) and poly(2-vinylpyridine) (P2VP) can be tuned through P3DDT regioregularity (RR), as this attribute controls the melting temperature and crystallization rates of P3DDT. When RR is low (70-80%), crystallization is

observed at temperatures near or below the glass transition of P2VP, so crystal growth is largely confined by the glassy cylindrical or lamellar BCP structure. When RR is high (94%), crystallization occurs at 40 K above the glass transition of P2VP, so there is no longer a restriction of glassy domains. Importantly, crystal growth remains confined by the rubbery P2VP lamellae, but breaks through the rubbery P2VP cylinders. This morphology-dependent behavior is attributed to geometric compatibility of P3DDT crystal growth and the self-assembled symmetry: In a lamellar phase, the P3DDT chain orientations at the P3DDT-*block*-P2VP interface are compatible with crystal growth, and both the alkyl-stacking and π - π growth directions are unrestricted within a lamellar sheet. In a cylindrical phase, the radial orientation of P3DDT chains at the P3DDT-*block*-P2VP interface is not compatible with crystal growth, and the hexagonal close-packed symmetry only allows for one direction of unrestricted crystal growth. Significantly, these studies demonstrate that tuning RR of polyalkylthiophenes can open up multiple crystallization modes with the same monomer chemistries and block lengths, thereby decoupling the parameters that govern classical BCP self-assembly and crystal growth.

Introduction

Conjugated polymers have unique optoelectronic properties that enable their applications in photovoltaics, batteries, light-emitting diodes, and field effect transistors.¹⁻⁵ When conjugated polymers are incorporated in a block copolymer (BCP) architecture, their utility and functions can be enhanced by self-assembly: as examples, the formation of nanoscale functional domains and high interfacial area can tune charge and energy transfer processes^{6,7} or tailor mechanical responses.^{8,9} However, it is well-documented that crystallization of conjugated blocks can disrupt self-assembly, leading to a poorly-ordered fibrillar texture. This behavior has been observed in conjugated-coil BCPs based on highly regioregular poly(3-hexylthiophene) (P3HT)¹⁰⁻¹³ and poly(2,5-di(2'-ethylhexyloxy)-1,4-phenylenevinylene).¹⁴

In polyethylene-based BCPs, it is possible to crystallize polyethylene while maintaining all or some of the self-assembled structure. This is achieved through processes termed “confined” and “templated” crystallization.^{15–17} In confined crystallization, confinement is imposed in one of two ways: the amorphous block is glassy at the crystallization temperature, producing a physical boundary that guides crystallization within the self-assembled structure;^{18–20} or the amorphous block is rubbery at the crystallization temperature, yet the BCP is so strongly segregated that thermodynamic barriers prevent changes to the self-assembled structure during crystal growth.¹⁵ Templated crystallization is observed when the amorphous block is rubbery and the copolymer is at intermediate segregation strength, so crystal growth can distort the domains, but the overall self-assembled symmetry is preserved.^{15,21} Finally, polyethylene-based BCPs can also undergo a “break out” crystallization process: this is observed when the amorphous block is rubbery and the BCP is more weakly segregated, so crystal growth destroys the melt state symmetry.^{15,22,23}

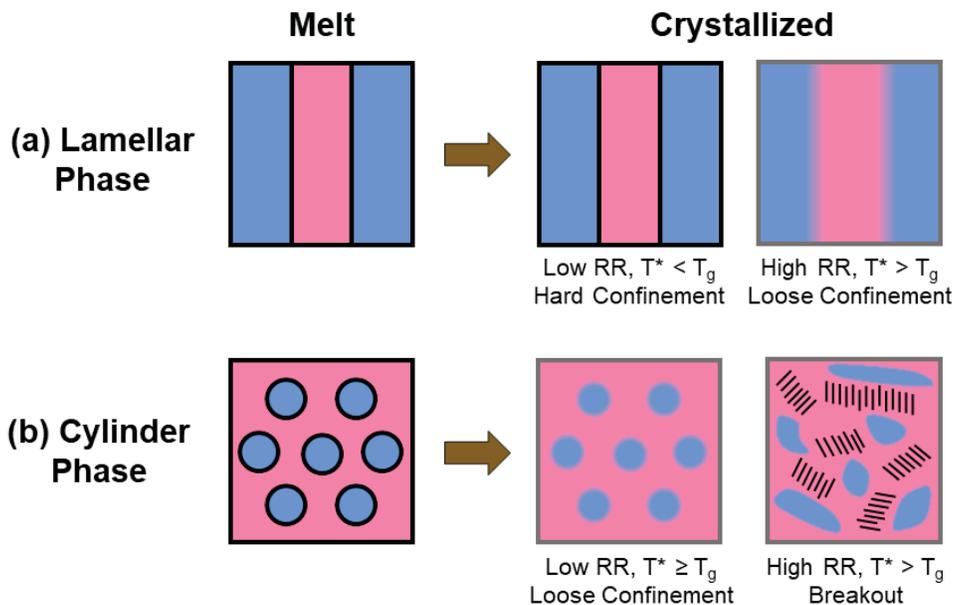
Poly(3-alkylthiophenes) (P3ATs) are a popular class of conjugated polymers for fundamental studies of structure-property relations,⁴ and show promise for applications in stretchable and wearable electronics.^{8,24–27} P3ATs and polyethylene (PE) have distinct chain conformations that lead to different crystallization mechanisms.²⁸ P3ATs are semiflexible polymers that adopt highly extended chain conformations in a melt state and during crystallization, so crystal growth is largely determined by intermolecular interactions. On the other hand, PE is very flexible and will fold during crystallization, so crystal growth proceeds by both intra- and inter-molecular processes. Despite these differences, it is possible to engineer P3AT-based BCPs that exhibit similar crystallization modes as PE-based BCPs. This is usually accomplished by using bulky alkyl substituents that increase the flexibility of conjugated blocks and reduce the strength of their intermolecular interactions, such that the drive for crystallization and self-assembly is more balanced. Confined crystallization has been demonstrated with lamellar and cylindrical BCPs based on highly regioregular poly(3-(2'-ethyl)hexylthiophene) (P3EHT) and flexible blocks such as poly(lactid acid) (PLA),²⁹

poly(ethylene oxide) (PEO),³⁰ poly(methyl acrylate) (PMA),^{31,32} and polystyrene (PS).³¹ Break-out crystallization has also been documented in P3EHT-PEO BCPs when the melt-state morphology is a gyroid, as this symmetry is not compatible with the P3EHT crystal growth.³⁰ Confined crystallization has also been demonstrated with BCPs based on highly regioregular poly(3-dodecylthiophene) (P3DDT) and poly(methyl methacrylate) when the P3DDT content was low (less than $\sim 60\%$), or the P3DDT block length was very high.^{33,34} Otherwise, break-out of P3DDT crystals destroys the self-assembled morphology.

While systematic changes to alkyl substituents can manipulate chain flexibility and interaction strength in P3ATs,³⁵ this approach will also change other attributes of the system, including the crystal structure and intrinsic electronic properties.³⁶ Furthermore, in P3AT-based BCPs, the Flory interaction parameter and conformational asymmetry will vary with the type of alkyl substituent. As an alternative, regioregularity (RR) can tune the chain flexibility and interaction strength of P3ATs,³⁵ and recent studies have shown that this attribute can be varied systematically in both P3HT and P3DDT.^{13,24,37} By controlling the RR of P3AT-based BCPs, one can decouple many of the architectural and thermodynamic parameters that control P3AT crystallization and self-assembly. This approach was first demonstrated with P3HT-*b*-poly(2-vinylpyridine): highly ordered lamellar and cylindrical BCP were observed when RR was less than approximately 80%, but crystal growth disrupted self-assembly when RR was high.¹³ However, highly regioregular P3HT has a very high melting temperature ($> 220^\circ\text{C}$), so it is difficult to access the melt-state morphology and examine crystallization behavior.

Recently, we reported the synthesis and melt-state structure in a series of P3DDT-*b*-poly(2-vinyl pyridine) (P2VP) materials.³⁷ These studies are enabled by the low P3DDT melting temperature of approximately 140°C at high RR. When RR is low (70-85%), the P3DDT chains adopt a bilayer conformation that is typical of flexible BCPs. However, when RR is high (94%), the P3DDT chains interdigitate in a liquid crystalline monolayer. These behaviors are observed in both lamellar (ca. 50% P3DDT) and cylindrical (ca. 70%

P3DDT) phases. In addition to changes in persistence length that might cause a material to transition from bilayer to liquid crystalline structure, changes in RR can also affect degree of crystallization and melting temperature of the P3DDT block, as well as crystallization modes within a block copolymer template. In our present work, we examine the effects of RR on crystallization modes of P3DDT-*b*-P2VP copolymers using time-resolved small angle and wide angle X-ray scattering. All samples are cooled from a melt state to below the crystallization temperature, and then isothermally annealed to examine crystal growth and any changes to the self-assembled structure. We find three different crystallization modes (Scheme 1) that are similar to the processes in PE-based materials: When lamellar and cylindrical phases are crystallized near or below the glass transition of P2VP, which occurs in systems with low RR, the crystal growth is confined by the block copolymer template. However, when crystallized above the glass transition of P2VP, we observe “loose confinement” in lamellar phases and breakout in cylindrical phases.



Scheme 1: Observed crystallization modes depend on both morphology and T^* relative to T_g , where T^* is defined as the highest temperature at which crystallization is detected in the WAXS spectrum after 2 minutes of isothermal annealing. T^* is sensitive to RR. Blue domains = P2VP.

Methods

Materials. All commercial solvents and chemicals used in this study were purchased from Merck Co. and Alfa Aesar Co. and used as received without further purification. All P3DDT-*b*-P2VP copolymers were prepared according to synthetic procedures in our previous work.³⁷ All of the synthetic details and characterization of RR-tuned P3DDT-*b*-P2VP are described in the Supporting Information.

Sample Preparation. All P3DDT-*b*-P2VP copolymers were prepared for X-ray scattering by pressing in aluminum low mass (10 μ L) DSC pans. The pans were placed in open glass vials for identification and annealed under high vacuum (10^{-7} Torr) at 160 °C overnight (10-15 hr).

Small Angle/Wide Angle X-ray Scattering (SAXS/WAXS). Simultaneous small-angle X-ray scattering (SAXS) and wide-angle X-ray scattering (WAXS) measurements were performed at the beamline 12-ID-B at Argonne National Laboratory. The DSC pans holding pre-annealed samples were fit into a Linkam heating stage and illuminated at normal incidence (transmission through the film thickness) under nitrogen at temperatures ranging from 160 °C down to 25 °C. Feedback to the temperature controller came from a thermocouple embedded in the stage, and a secondary thermocouple measured the temperature at the inserted DSC pan. Temperature stability was considered to be the point at which these two thermocouples recorded the same value. Samples were probed with a 13.3 keV (wavelength $\lambda = 0.093$ nm) X-ray beam with a sample to detector distance of 2.3 m using a 0.1 sec exposure time. The beam spot size at the sample was approximately 10 μ m tall by 200 μ m wide. To avoid beam damage, the position relative to the beam was changed by 11 μ m along the vertical direction between every exposure. Scattered radiation was collected using a Pilatus 2M detector (1475 \times 1679 pixels, 172 μ m pixel size). The 2-dimensional (2D) scattering data were reduced to 1-dimensional (1D) scattering curves by azimuthal integration using the

SAXSLee software. Scattering data were collected for an empty aluminum DSC pan under nitrogen at ambient conditions to act as a background measurement. The scattering data for samples were corrected by subtracting this background measurement. The magnitude of the scattering vector (q) is given by $q = 4\pi \sin \theta / \lambda$, where 2θ is the scattering angle. The q -range detected was 0.04 to 2.7 nm⁻¹. Direct beam transmission intensity was recorded with a photodiode and was then used to calculate the sample thickness at each measurement spot using the equation $x = -\ln(I_0/I)$, where x is the sample thickness at the measurement spot, I_0 is the direct beam intensity prior to transmission, and I is the direct beam intensity after transmission. The scattered intensity I_s collected for each spot at the Pilatus detector was then corrected by normalizing with the thickness x , i.e., I_s/x .

Transmission Electron Microscopy (TEM). Samples were prepared for TEM by annealing at 200 °C for 2 hr then slowly cooling to 160 °C and annealing for 24 hr. Samples were then cooled to room temperature over 24 hr at a constant cooling rate of 0.09 °C/min. (The annealing procedure for TEM samples differed from that of scattering samples because a longer annealing time enhances the cylindrical order and improves image quality.) Samples were microtomed to ~50 nm thickness employing an RMC PowerTome-X with a diamond knife and then stained with iodine vapor. All the TEM images were obtained using a JEM-3011 HR electron microscope.

Results and discussion

The P3DDT-*b*-P2VP materials considered in this work are summarized in Table 1. All of the synthetic details and characterization of RR-tuned P3DDT-*b*-P2VP are described elsewhere³⁷ and briefly summarized in the Supporting Information. For convenience, the copolymers were denoted as RR*X*-VP*Y*, where *X* is the RR of P3DDT block and *Y* is the volume fraction of P2VP block. All are majority P3DDT and assemble into either lamellar or hexagonally-packed cylindrical morphologies. Within each domain, the chain

packing depends on the P3DDT RR:³⁷ When RR is high, the chains interdigitate in a liquid crystalline monolayer (LC). Otherwise, the chains adopt a flexible bilayer conformation (BL). The Supporting Information Table S1 summarizes degree of crystallinity and melting temperatures for P3DDT homopolymers and P3DDT-b-P2VP, measured with DSC. These data demonstrate that degree of crystallinity and P3DDT melting temperature both increase with RR. These transitions were too weak to detect in some of the low RR samples, which is likely associated with the slow crystallization kinetics.

The crystallization temperature for SAXS/WAXS measurements was selected based on the rate of crystallization at a reference temperature T^* , which is the highest temperature where crystallization is detected after 2 min of isothermal annealing. We defined this reference temperature for convenience: very fast crystallization process cannot be examined under isothermal conditions due to finite cooling rates (maximum of 20 to 30 °C/min), and a very slow crystallization process is impractical due to time limitations at the synchrotron. T^* was determined by the following procedure: Each sample was first heated to 160 °C for about 8 min to melt any crystals present. The sample was then cooled by a few degrees and a measurement was taken after waiting two min at the new temperature. If there were no crystal peaks visible, then the cooling and waiting process was repeated until the (100) crystal peak for P3DDT was visible, which is the temperature T^* . Values of T^* for all samples are reported in Table 2. For all cylinder-forming samples, T^* was greater than or equal to the T_g of P2VP (95 °C). In the lamellar-forming samples, T^* was above T_g of P2VP only for the 94% RR samples. Once T^* was determined, the sample was heated again to 160°C for at least 8 min. When the crystal peaks were no longer detected in the WAXS spectrum, the sample was cooled to a set point of 5°C above T^* and held for 1.5 min, which minimizes lag between the set point and actual sample temperature, and then rapidly cooled to a target temperature T^e below T^* . SAXS and WAXS data were recorded every few sec until the intensity of the (100) peak reached a plateau.

A representative 1D plot of the scattering data from a single experiment is shown in

Table 1: Summary of Materials. RR is regioregularity of P3DDT block, determined by NMR; N is average degree of polymerization, determined by signal intensities and mass-to-charge ratios from MALDI-ToF for P3DDTs and SEC for P2VPs; f_{P2VP} is P2VP volume fraction, determined by NMR; \mathbb{D} is dispersity index, determined by SEC.

Sample Name	RR	N_{P3DDT}	N_{P2VP}	f_{P2VP}	$\mathbb{D}_{\text{P3DDT}}$	\mathbb{D}_{P2VP}
RR94-VP34	95	18	28	0.34	1.09	1.14
RR79-VP39	79	19	30	0.39	1.22	1.16
RR70-VP37	70	17	30	0.37	1.20	1.16
RR94-VP25	94	18	19	0.25	1.09	1.14
RR79-VP29	79	19	19	0.29	1.22	1.14
RR70-VP29	70	17	19	0.29	1.20	1.14

Table 2: Summary of Sample Characteristics. Structure is the self-assembled morphology in a melt state (BL = bilayer, LC = liquid crystal), determined by SAXS measurement at 160 °C; T_c^{DSC} and T_m^{DSC} are the P3DDT crystallization and melting temperature, respectively, determined by DSC. In some samples, DSC could not detect the crystallization or melting temperature.

Sample Name	Structure	T_c^{DSC}	T_m^{DSC}	T^*
RR94-VP34	LAM, LC	106.0	138.9	140
RR79-VP39	LAM, BL	77.8	128.7	85
RR70-VP37	LAM, BL	-	-	80
RR94-VP25	HPC, LC	108.8	134.4	140
RR79-VP29	HPC, BL	-	-	105
RR70-VP29	HPC, BL	-	-	95

Figure 1. The change in color from one curve to the next indicates the time elapsed since the first measurement was made, with the blues representing the shortest times and the reds the longest times. In the first measurements, when the temperature of the sample is still above the P3DDT melting temperature, the only peaks observed come from the characteristic periodicity of the lamellar or cylindrical self-assembled structure. For example, the short-time data in Figure 1 show the primary SAXS peak at $q = 0.027 \text{ \AA}^{-1}$ and three higher order peaks at integer multiples of this value, indicative of a lamellar structure with periodicity $d = 233 \text{ \AA}$. As time progresses and the temperature stabilizes below the P3DDT crystallization temperature, the crystalline peaks appear at high q and grow over time. The most prominent of these is the (100) diffraction peak at $q = 0.22 \text{ \AA}^{-1}$ that corresponds with the dodecyl side-chain stacking direction.³⁸⁻⁴⁰ The two weaker peaks at $q = 0.44$ and 0.66 \AA^{-1} are higher order multiples of the same direction, i.e., (200) and (300), respectively. In one sample, namely RR79-VP29, a diffraction peak corresponding to the (010) direction for pi-stacking of the thiophene rings can be observed at still higher q of about 1.6 \AA^{-1} . In most cases, however, this peak is not seen, likely due to its position coinciding with the broad amorphous halo from dodecyl side chains.

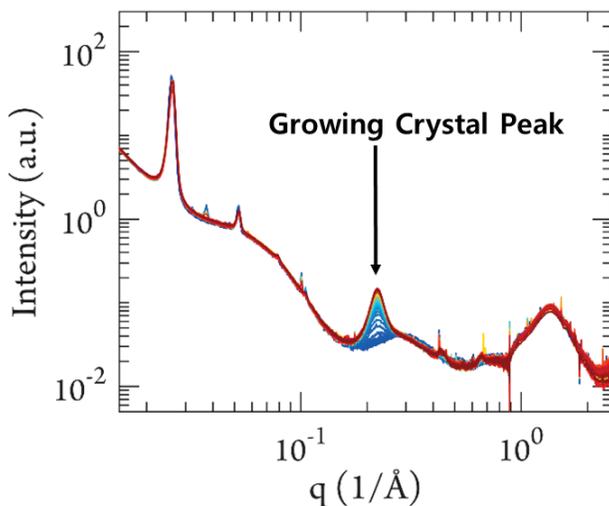


Figure 1: Scattering data for RR79-VP39. Measurements performed $75 \text{ }^\circ\text{C}$ (quenched from $160 \text{ }^\circ\text{C}$), beginning with blue and ending with red, with 2 sec elapsed between measurements.

The effects of P3DDT crystallization on P3DDT-*b*-P2VP self-assembly were examined by tracking the positions, shapes and integrated intensities of each SAXS and WAXS peak as a function of time. Each peak was fit to either a pseudo-Voigt approximation (first SAXS peak) or a Lorentzian function (all other SAXS and WAXS peaks). The trends in each parameter were consistent for both primary and higher-order peaks, so only the primary peak data for SAXS and WAXS are reported here. The center of each primary peak (q_1) is used to calculate the corresponding periodicity $d = 2\pi/q_1$. The breadth of each peak, which is reflected by the full width at half max Δ , reflects the size and extent of disorder in each block copolymer grain (SAXS) or P3DDT crystallite (WAXS). The integrated intensity I is proportional to the density of grains or crystallites within the samples. Three distinct crystallization modes are observed, and are controlled by both the self-assembled morphology and proximity of T^* to the T_g of P2VP (95°C).

In the first of the crystallization modes, for which T^* is below the T_g of P2VP, the P2VP domains are glassy and unable to give way to growing P3DDT crystals. This behavior, referred to here as “confined” crystallization, can be seen in the crystallization of the 79% RR lamellar sample (RR79-VP39, $T^* = 85^\circ\text{C}$) at 75°C (Figure 2). As crystallization proceeds, as indicated by the increased intensity of the primary WAXS peak (I^{WAXS}), both the lamellar domain periodicity (d^{SAXS}) and the the full-width half max (Δ^{SAXS}) of the primary SAXS peak remain essentially constant. This outcome demonstrates that the hierarchical organization of the lamellae is unchanged through crystallization. The variation in intensity of the primary SAXS peak in RR79-VP39 is correlated with different sample positions. We correct for changes in thickness among different samples positions, so the fluctuations reflect spatial heterogeneities that are more significant in RR79-VP39 than in other samples. Though not shown here, the confined behavior is also observed for crystallization of the 70% RR lamellar sample (RR70-VP37) at 70°C .

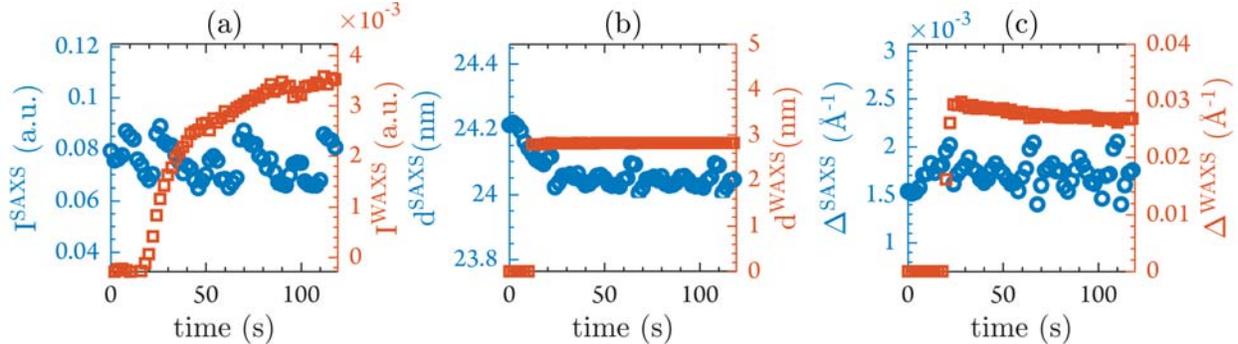


Figure 2: Change in (a) intensity of primary SAXS and WAXS peaks, (b) domain spacing of SAXS (lamellae) and WAXS (P3DDT crystal) structure, and (c) full width half max of SAXS and WAXS peaks for lamellae-forming sample RR79-VP39, with respect to time.

The second crystallization mode, referred to here as “loose confinement” behavior, is characterized by an overall retention of the self-assembled symmetry, but with subtle changes in average domain periodicity and grain structure as crystallization progresses. Loosely confined crystallization is observed when T^* is very near the T_g of P2VP in the cylindrical samples, and when T^* is near or significantly above the T_g of P2VP in the lamellar sample. This behavior is shown in Figure 3 for the 94% RR lamellar and 79% RR cylinder-forming samples: lamellar RR-94-VP34 at 140°C and cylindrical RR79-VP29 at 105°C . As crystallization proceeds, both samples experience changes in the domain periodicity (d^{SAXS}) and an increase in the full width half max of the primary SAXS peak (Δ^{SAXS}), but the intensity of the primary SAXS peak (I^{SAXS}) remains fairly constant. This indicates that the growing crystals can disrupt the melt morphology, but they do not destroy it altogether. When T^* is near T_g of P2VP, it is possible that slow diffusivity inhibits rearrangements in the nanoscale structure. However, when T^* is much larger T_g of P2VP in the lamellar RR-94-VP34 sample, the loosely confined behavior does not reflect a diffusion limited process. The characteristics of this process are similar to the templated mode reported in rubbery PE-based block copolymers of intermediate segregation strength.¹⁵

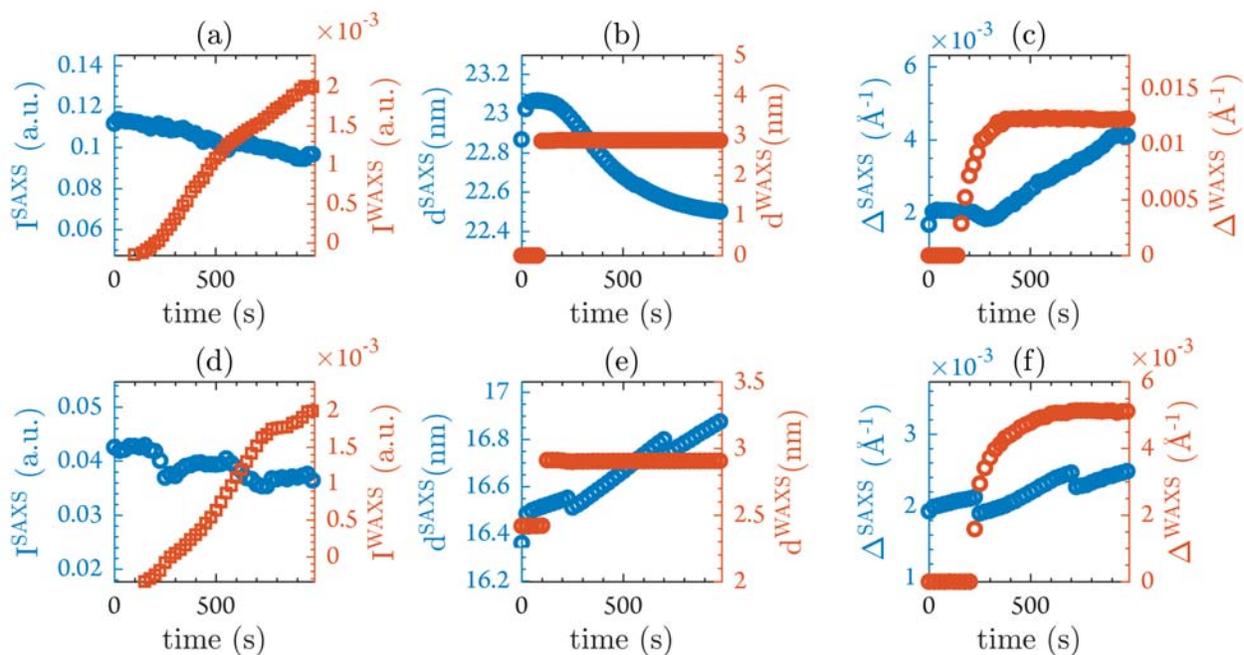


Figure 3: Change in (a) intensity of primary SAXS and WAXS peaks, (b) domain spacing of SAXS (lamellae) and WAXS (P3DDT crystal) structure, and (c) full width half max of SAXS and WAXS peaks for cylinder-forming sample RR79-VP29, with respect to time. The same data are shown for lamellae-forming RR94-VP34 (d, e, f).

It is interesting to note that while the domain spacing increases in the 94% RR sample shown in Figure 3 (RR94-VP34), the domain spacing decreases in the 79% RR samples. This can be explained by the difference in packing of the P3DDT chains between the 94% and lower RRs. It has been previously shown that BCPs of P2VP and 94% RR P3DDT exhibit a high degree of chain interdigitation, forming a liquid crystalline monolayer.^{37,41} BCPs with low RR, on the other hand, exhibit the bilayer chain packing that is typical of flexible BCP systems. Crystal growth in the tightly-packed liquid crystalline monolayer may promote further chain extension, thereby swelling the domain sizes and increasing the periodicity.⁴¹ However, in the bilayer conformation, crystallization will increase the P3DDT density and produce domain contraction.¹⁹

The third of the observed crystallization modes is breakout, and is seen only in the cylinder-forming sample for which T^* is significantly higher than the T_g of P2VP. In this mode, the growing crystals disrupt the self-assembled morphology, as indicated by a decrease

in intensity of the primary SAXS peaks coinciding with an increase in the intensity of the primary WAXS peak. There is also observed, as might be expected, a concurrent change in domain spacing and increase in full-width half max of the primary SAXS peak (Figure 4). The presence of the breakout mode is confirmed by TEM measurements. As shown in Figure 5, the self assembled structure is preserved in all samples except the 94% RR cylinder-forming sample: instead of the expected cylinders, this micrograph reveals small fibril-like crystal structures.

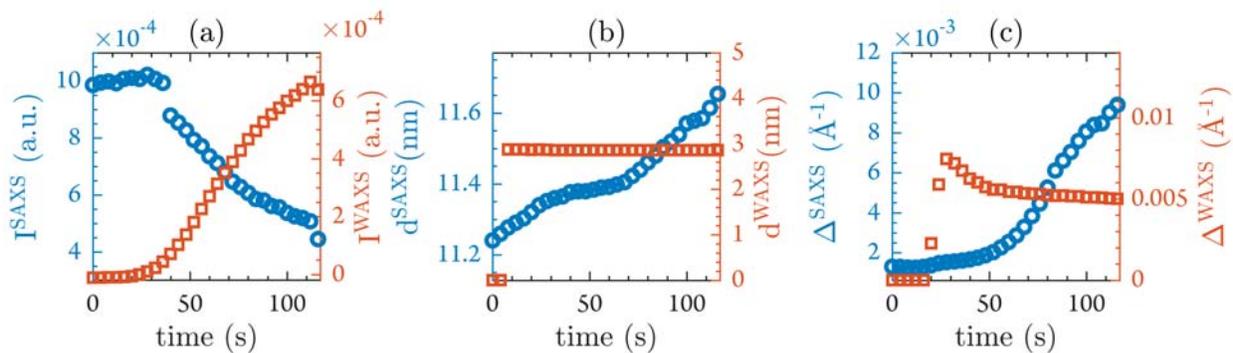


Figure 4: Change in (a) intensity of primary SAXS and WAXS peaks, (b) domain spacing of SAXS (cylinders) and WAXS (P3DDT crystal) structure, and (c) full width half max of SAXS and WAXS peaks for sample RR94-VP25, with respect to time.

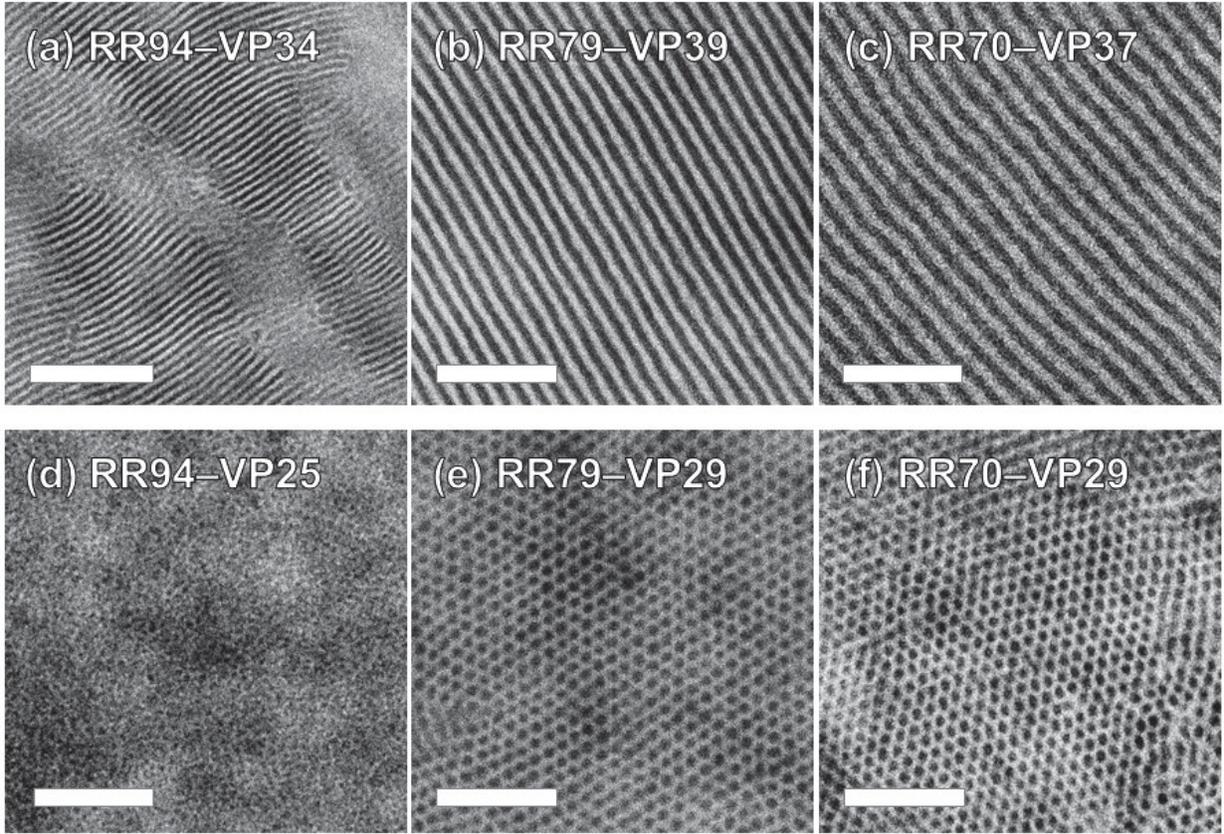


Figure 5: Cross-sectional TEM images of (a) RR94-VP34; (b) RR79-VP39; (c) RR70-VP37; (d) RR94-VP25; (e) RR79-VP29; (f) RR70-VP29. P2VP domains were selectively stained dark by exposure to iodine vapor. The scale bars are 200 nm.

The 94% RR lamellar (RR94-VP34) and cylindrical (RR94-VP25) samples were both examined at crystallization temperatures well above the T_g of P2VP, but they exhibit different crystallization modes. There are two likely underlying causes for the distinct behaviors. The first explanation relates to geometric frustration, as illustrated in Figure 6: In a lamellar structure, the P3DDT chain orientations and crystal symmetry are compatible with the natural dimensions of a lamellar sheet, so crystals can grow along both the (100) alkyl-stacking and (010) π - π stacking directions without restriction. In the hexagonal close-packed arrangement of cylindrical domains, the P3DDT chains radiate out from the cylinder center. Crystallization will therefore disrupt curvature at the P3DDT-*b*-P2VP interface, and the only unrestricted direction for crystal growth is along the length of the cylinders. In BCPs

of poly(3-(2'-ethyl)hexylthiophene) (P3EHT) and poly(methyl acrylate) in which P3EHT is the minority block, the crystals tend to align with the (100) direction along the cylinder axis.³² If the same holds true for the P3DDT-based BCPs, then growth along the (010) π - π stacking direction competes with the natural hexagonal symmetry, and the maximum crystallite size along this direction that could “fit” in the lattice is $2d$, where $d = 11.3$ nm for 94% RR (RR94-VP25). The second possible explanation is that the lamellar sample is more strongly segregated than the cylinder sample. In a typical flexible BCP system, the order-disorder transition for a lamellar-forming polymer occurs at lower values of χN than it does for a cylinder-forming polymer, and the minimum segregation strength for confined crystallization can vary with morphology.¹⁵ Both of these samples have relatively low values of N , so it is possible that the state of the cylindrical sample is much closer to the order-disorder transition than the lamellar sample. This is difficult to test experimentally, as no order-disorder transition is detected for a cylindrical specimen (RR79-VP29) after heating up to 240°C, so the system is either strongly segregated or the χ -parameter is not sensitive to temperature. Finally, the degree of crystallinity in RR95-VP25 (cylinders) is higher than RR95-VP34 (lamellae), as noted in Table S1. It is unclear if this is a cause or effect of different crystallization modes.

We note that samples with RR below 94% did not crystallize to a measurable extent unless cooled near the T_g of P2VP. Therefore, these experiments do not offer insight into the role of a liquid crystalline monolayer (RR 94%) versus a flexible bilayer (RR 70 and 79%) on the breakout process. Such packing effects could be interrogated by replacing P2VP with a polymer that has a lower T_g , which is the subject of ongoing work.

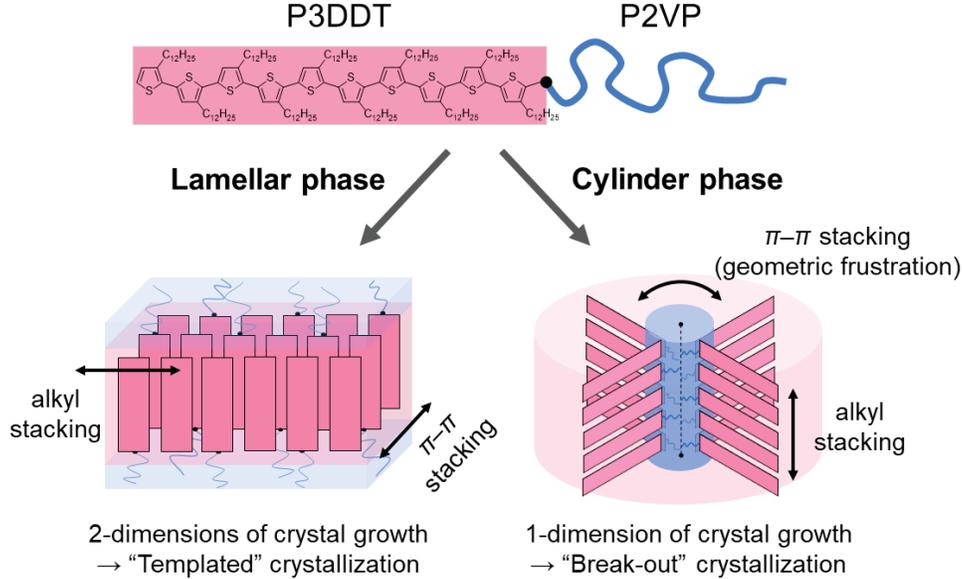


Figure 6: An illustration of the possible geometric explanation for the difference in crystallization mode between the 94% RR lamellar and cylinder samples.

Conclusions

We examine the crystallization modes in P3DDT-*b*-P2VP copolymers as functions of copolymer composition and P3DDT RR. All materials have a majority P3DDT composition and assemble into ordered lamellae or cylinders when annealed above the P3DDT. As the materials are quenched below the P3DDT T_m , the crystallization process and self-assembled morphology are monitored with simultaneous SAXS and WAXS. At T^* below the P2VP glass transition, the crystal growth is confined by the glassy P2VP domains. At T^* near the P2VP glass transition, the crystal growth perturbs the self-assembled morphology, but there is no large-scale destruction of the lamellae or cylinders. While the characteristics of this process are similar to the templated growth mode that is observed in other semicrystalline BCP systems, there may be diffusion barriers at these low temperatures that inhibit rearrangements of the nanoscale domains, leading to behavior that is better described as loose confinement. At T^* well-above the P2VP glass transition, the crystallization mode depends on the BCP morphology. In a lamellar phase, crystal growth and self-assembly can coexist. However, in

a cylindrical phase, the crystallites ultimately break-out of the self-assembled structure. As the lamellar and cylindrical materials have very similar molecular weights, we propose that break-out in the cylindrical morphology is associated with mismatch between the natural dimensions of the BCP and P3DDT lattices. It is also possible that the segregation strength of cylinder-forming materials is not high enough for confined crystallization. Significantly, these studies demonstrate that tuning RR of poly(3-alkylthiophenes) can open up multiple crystallization modes with the same monomer chemistries and molecular weights. This approach can decouple the parameters that govern classical BCP self-assembly (segregation strength χN , volume fraction f) and interactions between conjugated blocks (Maier-Saupé parameter μN , persistence length L_p), providing a model system for fundamental studies of crystallization in conjugated BCP.

Acknowledgement

J.P.C., and G.E.S. acknowledge financial support from the National Science Foundation under Award No. DMR-1731292. This research used resources of the Advanced Photon Source, an Office of Science User Facility operated for the U.S. Department of Energy (DOE) by Argonne National Laboratory under Contract No. DE-AC02-06CH11357. This work was supported by the KETEP and the MOTIE of the Republic of Korea (20163030013620 and 20163010012470). We acknowledge additional support for this work from the Research Projects of the KAIST-KUSTAR.

Supporting Information Available

The Supporting Information is available free of charge on the ACS Publications website at DOI:10.1021. Polymer synthesis and characterization; time-resolved SAXS and WAXS data for each sample.

References

- (1) Morris, M. A.; An, H.; Lutkenhaus, J. L.; Epps, T. H. Harnessing the Power of Plastics: Nanostructured Polymer Systems in Lithium-Ion Batteries. *ACS Energy Lett.* **2017**, *2*, 1919–1936, DOI: 10.1021/acsenergylett.7b00368.
- (2) Swager, T. M. 50th Anniversary Perspective: Conducting/Semiconducting Conjugated Polymers. A Personal Perspective on the Past and the Future. *Macromolecules* **2017**, *50*, 4867–4886, DOI: 10.1021/acs.macromol.7b00582.
- (3) Facchetti, A. π -Conjugated Polymers for Organic Electronics and Photovoltaic Cell Applications. *Chem. Mater.* **2011**, *23*, 733–758, DOI: 10.1021/cm102419z.
- (4) Kaloni, T. P.; Giesbrecht, P. K.; Schreckenbach, G.; Freund, M. S. Polythiophene: From Fundamental Perspectives to Applications. *Chem. Mater.* **2017**, *29*, 10248–10283, DOI: 10.1021/acs.chemmater.7b03035.
- (5) Kang, H.; Lee, W.; Oh, J.; Kim, T.; Lee, C.; Kim, B. J. From Fullerene-Polymer to All-Polymer Solar Cells: The Importance of Molecular Packing, Orientation, and Morphology Control. *Acc. Chem. Res.* **2016**, *49*, 2424–2434, DOI: 10.1021/acs.accounts.6b00347.
- (6) Segalman, R. A.; McCulloch, B.; Kirmayer, S.; Urban, J. J. Block Copolymers for Organic Optoelectronics. *Macromolecules* **2009**, *42*, 9205–9216, DOI: 10.1021/ma901350w.
- (7) Lee, Y.; Gomez, E. D. Challenges and Opportunities in the Development of Conjugated Block Copolymers for Photovoltaics. *Macromolecules* **2015**, *48*, 7385–7395, DOI: 10.1021/acs.macromol.5b00112.
- (8) Wang, S.; Oh, J. Y.; Xu, J.; Tran, H.; Bao, Z. Skin-Inspired Electronics: An Emerging Paradigm. *Acc. Chem. Res.* **2018**, *51*, 1033–1045, DOI: 10.1021/acs.accounts.8b00015.

- (9) Kim, H. J.; Kim, J.-H.; Ryu, J.-H.; Kim, Y.; Kang, H.; Lee, W. B.; Kim, T.-S.; Kim, B. J. Architectural Engineering of Rod-Coil Compatibilizers for Producing Mechanically and Thermally Stable Polymer Solar Cells. *ACS Nano* **2014**, *8*, 10461–10470, DOI: 10.1021/nn503823z.
- (10) Botiz, I.; Darling, S. B. Self-Assembly of Poly(3-hexylthiophene)-block-poly(lactide) Block Copolymer and Subsequent Incorporation of Electron Acceptor Material. *Macromolecules* **2009**, *42*, 8211–8217, DOI: 10.1021/ma901420h.
- (11) Wang, J.-T.; Takshima, S.; Wu, H.-C.; Shih, C.-C.; Isono, T.; Kakuchi, T.; Satoh, T.; Chen, W.-C. Stretchable Conjugated Rod-Coil Poly(3-hexylthiophene)-*block* -poly(butyl acrylate) Thin Films for Field Effect Transistor Applications. *Macromolecules* **2017**, *50*, 1442–1452, DOI: 10.1021/acs.macromol.6b02722.
- (12) Wu, Z.-Q.; Ono, R. J.; Chen, Z.; Bielawski, C. W. Synthesis of Poly(3-alkylthiophene)-block-poly(arylisocyanide): Two Sequential, Mechanistically Distinct Polymerizations Using a Single Catalyst. *J. Am. Chem. Soc.* **2010**, *132*, 14000–14001, DOI: 10.1021/ja106999q.
- (13) Kim, J.-S.; Kim, Y.; Kim, H.-J.; Kim, H. J.; Yang, H.; Jung, Y. S.; Stein, G. E.; Kim, B. J. Regioregularity-Driven Morphological Transition of Poly(3-hexylthiophene)-Based Block Copolymers. *Macromolecules* **2017**, *50*, 1902–1908, DOI: 10.1021/acs.macromol.7b00128.
- (14) Olsen, B. D.; Alcazar, D.; Krikorian, V.; Toney, M. F.; Thomas, E. L.; Segalman, R. A. Crystalline Structure in Thin Films of DEH-PPV Homopolymer and PPV-b-PI Rod-Coil Block Copolymers. *Macromolecules* **2008**, *41*, 58–66, DOI: 10.1021/ma0714971.
- (15) Loo, Y.-L.; Register, R. A.; Ryan, A. J. Modes of Crystallization in Block Copolymer Microdomains: Breakout, Templated, and Confined. *Macromolecules* **2002**, *35*, 2365–2374, DOI: 10.1021/ma011824j.

- (16) Xu, J.-T.; Turner, S. C.; Fairclough, J. P. A.; Mai, S.-M.; Ryan, A. J.; Chaibundit, C.; Booth, C. Morphological Confinement on Crystallization in Blends of Poly(oxyethylene-block-oxybutylene) and Poly(oxybutylene). *Macromolecules* **2002**, *35*, 3614–3621, DOI: 10.1021/ma0116147.
- (17) Burns, A. B.; Register, R. A. Large, Reversible, and Coherent Domain Spacing Dilation Driven by Crystallization under Soft Lamellar Confinement. *Macromolecules* **2017**, *50*, 8106–8116, DOI: 10.1021/acs.macromol.7b01632.
- (18) Zhu, L.; Cheng, S. Z. D.; Calhoun, B. H.; Ge, Q.; Quirk, R. P.; Thomas, E. L.; Hsiao, B. S.; Yeh, F.; Lotz, B. Crystallization Temperature-Dependent Crystal Orientations within Nanoscale Confined Lamellae of a Self-Assembled Crystalline-Amorphous Diblock Copolymer. *J. Am. Chem. Soc.* **2000**, *122*, 5957–5967, DOI: 10.1021/ja000275e.
- (19) Loo, Y.-L.; Register, R. A.; Ryan, A. J.; Dee, G. T. Polymer Crystallization Confined in One, Two, or Three Dimensions. *Macromolecules* **2001**, *34*, 8968–8977, DOI: 10.1021/ma011521p.
- (20) Xu, J.-T.; Yuan, J.-J.; Cheng, S.-Y. SAXS/WAXS/DSC studies on crystallization of a polystyrene-b-poly(ethylene oxide)-b-polystyrene triblock copolymer with lamellar morphology and low glass transition temperature. *Eur. Polym. J.* **2003**, *39*, 2091–2098, DOI: 10.1016/S0014-3057(03)00155-1.
- (21) Tong, Z.-Z.; Zhou, B.; Huang, J.; Xu, J.-T.; Fan, Z.-Q. Regulation of Crystallization Kinetics, Morphology, and Mechanical Properties of Olefinic Blocky Copolymers. *Macromolecules* **2014**, *47*, 333–346, DOI: 10.1021/ma4023263.
- (22) Wen, T.; Liu, G.; Zhou, Y.; Zhang, X.; Wang, F.; Chen, H.; Loos, J.; Wang, D. Epitaxy-Induced Crystallization of Olefin Block Copolymers. *Macromolecules* **2012**, *45*, 5979–5985, DOI: 10.1021/ma300619f.

- (23) Ho, R.-M.; Chang, C.-C.; Chung, T.-M.; Chiang, Y.-W.; Wu, J.-Y. Competition between microphase separation and crystallization in self-assembly sPS/PS-PEP blends. *Polymer* **2003**, *44*, 1459–1467, DOI: 10.1016/S0032-3861(03)00012-0.
- (24) Kim, J.-S.; Kim, J.-H.; Lee, W.; Yu, H.; Kim, H. J.; Song, I.; Shin, M.; Oh, J. H.; Jeong, U.; Kim, T.-S.; Kim, B. J. Tuning Mechanical and Optoelectrical Properties of Poly(3-hexylthiophene) through Systematic Regioregularity Control. *Macromolecules* **2015**, *48*, 4339–4346, DOI: 10.1021/acs.macromol.5b00524.
- (25) Wang, G.-J. N.; Gasperini, A.; Bao, Z. Stretchable Polymer Semiconductors for Plastic Electronics. *Adv. Electron. Mater.* *4*, 1700429, DOI: 10.1002/aelm.201700429.
- (26) Kim, H. J.; Lee, M. Y.; Kim, J.-S.; Kim, J.-H.; Yu, H.; Yun, H.; Liao, K.; Kim, T.-S.; Oh, J. H.; Kim, B. J. Solution-Assembled Blends of Regioregularity-Controlled Polythiophenes for Coexistence of Mechanical Resilience and Electronic Performance. *ACS Appl. Mater. Interfaces* **2017**, *9*, 14120–14128, DOI: 10.1021/acsami.6b16703.
- (27) Choi, D.; Kim, H.; Persson, N.; Chu, P.-H.; Chang, M.; Kang, J.-H.; Graham, S.; Reichmanis, E. Elastomer-Polymer Semiconductor Blends for High-Performance Stretchable Charge Transport Networks. *Chem. Mater.* **2016**, *28*, 1196–1204, DOI: 10.1021/acs.chemmater.5b04804.
- (28) Liu, J.; Arif, M.; Zou, J.; Khondaker, S. I.; Zhai, L. Controlling Poly(3-hexylthiophene) Crystal Dimension: Nanowhiskers and Nanoribbons. *Macromolecules* **2009**, *42*, 9390–9393, DOI: 10.1021/ma901955c.
- (29) Ho, V.; Boudouris, B. W.; McCulloch, B. L.; Shuttle, C. G.; Burkhardt, M.; Chabynyc, M. L.; Segalman, R. A. Poly(3-alkylthiophene) Diblock Copolymers with Ordered Microstructures and Continuous Semiconducting Pathways. *J. Am. Chem. Soc.* **2011**, *133*, 9270–9273, DOI: 10.1021/ja2035317.

- (30) Patel, S. N.; Javier, A. E.; Beers, K. M.; Pople, J. A.; Ho, V.; Segalman, R. A.; Balsara, N. P. Morphology and Thermodynamic Properties of a Copolymer with an Electronically Conducting Block: Poly(3-ethylhexylthiophene)-block-poly(ethylene oxide). *Nano Lett.* **2012**, *12*, 4901–4906, DOI: 10.1021/nl302454c.
- (31) Davidson, E. C.; Beckingham, B. S.; Ho, V.; Segalman, R. A. Confined crystallization in lamellae forming poly(3-(2'-ethyl)hexylthiophene) (P3EHT) block copolymers. *J. Polym. Sci. B Polym. Phys.* **2015**, *54*, 205–215, DOI: 10.1002/polb.23904.
- (32) Davidson, E. C.; Segalman, R. A. Confined Crystallization within Cylindrical P3EHT Block Copolymer Microdomains. *Macromolecules* **2017**, *50*, 6128–6136, DOI: 10.1021/acs.macromol.7b01323.
- (33) Moon, H. C.; Bae, D.; Kim, J. K. Self-Assembly of Poly(3-dodecylthiophene)-block-poly(methyl methacrylate) Copolymers Driven by Competition between Microphase Separation and Crystallization. *Macromolecules* **2012**, *45*, 5201–5207, DOI: 10.1021/ma300902n.
- (34) Park, J.; Lee, K. S.; Choi, C.; Kwak, J.; Moon, H. C.; Kim, J. K. Effect of Molecular Weight on Competitive Self-Assembly of Poly(3-dodecylthiophene)-block-poly(methyl methacrylate) Copolymers. *Macromolecules* **2016**, *49*, 3647–3653, DOI: 10.1021/acs.macromol.6b00513.
- (35) McCulloch, B.; Ho, V.; Hoarfrost, M.; Stanley, C.; Do, C.; Heller, W. T.; Segalman, R. A. Polymer Chain Shape of Poly(3-alkylthiophenes) in Solution Using Small-Angle Neutron Scattering. *Macromolecules* **2013**, *46*, 1899–1907, DOI: 10.1021/ma302463d.
- (36) Himmelberger, S.; Duong, D. T.; Northrup, J. E.; Rivnay, J.; Koch, F. P. V.; Beckingham, B. S.; Stingelin, N.; Segalman, R. A.; Mannsfeld, S. C. B.; Salleo, A. Role of

- Side-Chain Branching on Thin-Film Structure and Electronic Properties of Polythiophenes. *Adv. Funct. Mater.* **2015**, *25*, 2616–2624, DOI: 10.1002/adfm.201500101.
- (37) Kim, J.-S.; Han, J.; Kim, Y.; Park, H.; Coote, J. P.; Stein, G. E.; Kim, B. J. Domain Structures of Poly(3-dodecylthiophene)-Based Block Copolymers Depend on Regioregularity. *Macromolecules* **2018**, *51*, 4077–4084, DOI: 10.1021/acs.macromol.8b00795.
- (38) Ho, V.; Boudouris, B. W.; Segalman, R. A. Tuning Polythiophene Crystallization through Systematic Side Chain Functionalization. *Macromolecules* **2010**, *43*, 7895–7899, DOI: 10.1021/ma101697m.
- (39) Prosa, T. J.; Winokur, M. J.; McCullough, R. D. Evidence of a Novel Side Chain Structure in Regioregular Poly(3-alkylthiophenes). *Macromolecules* **1996**, *29*, 3654–3656, DOI: 10.1021/ma951510u.
- (40) Lin, S.-H.; Ho, C.-C.; Su, W.-F. Cylinder-to-gyroid phase transition in a rod-coil diblock copolymer. *Soft Matter* **2012**, *8*, 4890–4893, DOI: 10.1039/c2sm07473g.
- (41) Davidson, E. C.; Segalman, R. A. Thermal Control of Confined Crystallization within P3EHT Block Copolymer Microdomains. *Macromolecules* **2017**, *50*, 8097–8105, DOI: 10.1021/acs.macromol.7b01616.

Graphical TOC Entry

